Research Article

Operando XAS and DFT Uncover Structure-Performance Relationships in Re/TiO$_2$ for Selective CO$_2$ Hydrogenation to Methanol

Maite Lippel Gothe,* Adriano Henrique Braga, Lais Reis Borges, Jiyun Hong, Giliandro Farias, Alvaro David Torrez Baptista, Bryan Alberto Laura Larico, Ana Barbara Moulin Cansian, Caetano Rodrigues Miranda, Simon R. Bare, Liane Marcia Rossi, and Pedro Vidinha*

Read Online

| ACCESS | Metrics & More | Article Recommendations | Supporting Information |

ABSTRACT: The conversion of CO$_2$ into value-added chemicals, such as methanol, offers a promising pathway toward a renewable energy future. However, a precise kinetic control and a highly selective catalyst are necessary to overcome the thermodynamic preference for CO$_2$ hydrogenation to methane. Rhenium-based catalysts, particularly Re/TiO$_2$, demonstrate high activity and selectivity for methanol under high-pressure conditions. For example, at 100 bar and 200 °C, a methanol selectivity of 97−99% was obtained. Catalysts with 1 wt % Re and 5 wt % Re/TiO$_2$ were used to study the effect of cluster sizes. At 250 °C, the 1 wt % catalyst achieves 97% selectivity at 23% conversion, whereas 5 wt % Re/TiO$_2$ achieves 74% selectivity at 40% conversion, corresponding to a drop in space-time yield from 65 to 16 g$_{CH_3OH}$·g$_{Re}^{-1}$·h^{-1}, respectively. X-ray absorption spectroscopy provided insights into the structure of the active sites, while density functional theory calculations revealed the effects of cluster size on the energy barriers for H$_2$ activation, CH$_3$OH dissociation, and CH$_3$OH desorption, all of which directly influence conversion and selectivity. These results underscore the importance of balancing cluster size for optimal catalyst performance and provide insights into the design of efficient and selective catalysts for renewable methanol production.

KEYWORDS: carbon dioxide, hydrogenation, XAS, rhenium, nanoparticles

INTRODUCTION

Methanol (CH$_3$OH), which can be directly obtained from CO$_2$ hydrogenation, is a promising platform molecule, as it can be used as a fuel or integrated into downstream valorization processes to produce gasoline, aviation fuel, or dimethyl ether.[1] Thermodynamically, CH$_4$ is by far the most favorable product of CO$_2$ hydrogenation, as its Gibbs energy delta is negative ($\Delta G_{298K} = -113$ kJ mol^{-1}) while CH$_3$OH is not a favored product ($\Delta G_{298K} = 3.5$ kJ mol^{-1}). The thermodynamic equilibrium constant of the CO$_2$ to CH$_3$OH reaction ($K_{298K} = 2.45 \times 10^{-1}$) is 20 orders of magnitude lower than that of CO$_2$ to CH$_4$ ($K_{298K} = 7.79 \times 10^{19}$).[2] Even though high pressure and low temperature favor methanol, the selectivity of the CO$_2$ hydrogenation at the thermodynamic equilibrium is >99% selective to CH$_4$.[3−5] Therefore, since the conversion of CO$_2$ to methanol must rely on kinetic influences in order to be selective, a suitable catalyst is paramount for the feasibility of this process.[6]

In the hydrogenation of CO$_2$ to methanol, Cu, In, and Pd are more commonly identified as active metals in heterogeneous catalysts.[7] The copper−zinc-alumina mixed oxide catalysts, known as CZA, have been applied on industrial scale processes since the 1940s, and to date, with a reported CO$_2$ conversion of 20% and a selectivity of 40%.[8] A range of transition metals has been explored, with catalysts based on

In$_2$O$_3$ emerging as a highlight.[8−13] Particularly, a Pd/In$_2$O$_3$-SBA-15 catalyst reached 13% CO$_2$ conversion with 84% methanol selectivity.[14] In hydrogenation catalysis, rhenium has been recognized for its remarkable activity and selectivity in converting carboxylic acids into alcohols, as well as its low susceptibility to catalyst poisoning and deactivation.[15−21]

Rhenium catalysts have also been frequently studied in the hydrogenation of carbonyl and carboxyl groups, demonstrating high selectivity toward the formation of hydroxyl-functionalized products, avoiding overhydrogenation.[22−27] An efficient supercritical flow process for the hydrogenation of CO$_2$ to CH$_3$OH over a Re/TiO$_2$ catalyst has been reported by our group.[28] In the high-pressure hydrogenation of CO$_2$ to CH$_3$OH, the selectivity of rhenium-based catalysts is sensitive to small changes in their synthesis procedure, such as the choice of rhenium precursor or rhenium loading, as these

factors can affect the surface composition of the catalyst.[29] Additionally, recent literature suggests that catalysts composed of subnanometric clusters of rhenium on metal oxide supports present better methanol selectivity than catalysts composed of larger metallic nanoparticles, which lead to methanation.[30−32]

The efficiency and selectivity of CO_2 hydrogenation to methanol depend on the structural and electronic properties of the catalyst, which can be probed through a combination of experimental and computational techniques.[33,34] *In situ* and *operando* X-ray absorption spectroscopy (XAS) analyses of the active metal can be particularly helpful in the characterization of the active sites present,[35,36] and density functional theory (DFT) can provide additional insights to elucidate the catalytic performance of these materials.[37−39] Here, the supercritical flow process of CO_2 hydrogenation to CH_3OH over 1 or 5 wt % Re/TiO_2 was evaluated over a wide range of reaction conditions. DFT calculations of the dissociation of H_2 and CH_3OH on the surface of rhenium-based catalysts, coupled with *operando* XAS data, reveal how the size and structure of rhenium clusters—ranging from subnanometric to larger nanoparticles—affect the energetics and pathways of key reaction steps.

■ EXPERIMENTAL METHODS

Materials. Rhenium(VII) oxide (Re_2O_7) was purchased from Sigma-Aldrich at ≥99.9% purity, and titanium oxide P25 was purchased from Degussa at 99.9% purity and 20 nm particle size. Hydrogen gas and carbon dioxide were acquired from Special Gases at 99.5% purity. Carbon monoxide and methane analytical standards were acquired from White Martins at 99.99% purity. The analytical standard for methanol (CH_3OH) was obtained from Sigma-Aldrich at 99.999% purity. All single-way and double-way valves were purchased from a high-pressure company (HIP, USA). The high-pressure fixed-bed reactor used was produced in-house using stainless steel 316L and Swagelok fittings.

Catalyst Synthesis and Characterization. The Re/TiO_2 catalysts were synthesized by the wet impregnation of TiO_2 (P25, Degussa, 99.9%) with an aqueous solution of 0.1 mg mL^{-1} Re_2O_7 (Sigma-Aldrich, ≥99.9%). A suspension of 500 mg of TiO_2 support to 500 mL of Re_2O_7 aqueous solution was left under magnetic stirring overnight, followed by drying at 120 °C in air. Previous to the reactions, the Re/TiO_2 catalysts were heated under H_2 in order to reduce the rhenium oxide species to metallic rhenium clusters. The temperature of prereduction is specified for each experiment in the results discussion.

X-ray diffraction (XRD) patterns were obtained with a Rigaku Miniflex diffractometer using Cu Kα radiation, 30 kV tension, and 15 mA current, with a step 2θ of 0.01°. Rhenium percentages on the catalyst were evaluated by Inductively Coupled Plasma Optical Emission Spectrometry (ICP-OES) in a Spectro Arcos spectrometer. Samples were previously digested by heating in a 1:3 mixture of HNO_3 and HCl. Infrared (IR) spectrometry studies were performed using a Shimadzu IR Prestige 21 spectrometer, which measured spectra obtained from 64 scans at a spectral resolution of 4 cm^{-1}. A sample of 20 mg of Re/TiO_2 was pressed into a pellet and placed into a Specac IR high-temperature transmission cell. The catalyst was pretreated at 500 °C under a flow of 10 mL min^{-1} H_2 and 50 mL min^{-1} argon (Ar) before measurements. The reaction was studied by flowing 10 mL

min^{-1} of CO_2 and 30 mL min^{-1} of H_2 in 50 mL min^{-1} of Ar, at ambient pressure and several temperatures.

X-ray photoelectron spectroscopy (XPS) data were obtained with a Specs instrument with monochromatic Al Kα of excitation energy = 1486.71 eV. A constant pass energy of 40 eV and a step of 0.2 eV were applied to all high-resolution spectra, with a dwell time of 0.1 s. The number of scans acquired for Re 4f high-resolution spectra was 50 for the sample with 1 wt % Re and 30 for the sample with 5 wt % Re. For the high-resolution spectra of Ti 2p, 30 scans were sufficient for the analyses of both samples. CasaXPS software was used for peak fitting, and the well-defined Ti (IV) $2p_{3/2}$ peak was calibrated to 458.6 eV.

X-ray absorption spectroscopy (XAS) data at the Re L_3-edge (10535 eV) were measured at beamline 2−2 of the Stanford Synchrotron Radiation Lightsource (SSRL). Beamline 2−2 is the center branch of a bent magnet source with a water-cooled double-bounce monochromator equipped with a Si(220) crystal set. The XAS spectra were collected in continuous scanning mode with fluorescence detection using PIPS diode. The spectra of samples with 1 wt % rhenium were collected in a 180 s trajectory, while the spectra of samples with 5 wt % rhenium had a trajectory of 92 s. The samples were packed in a 1/8″ diameter quartz capillary tube as a fixed-bed reactor[40] to allow for the *in situ* XAS, coupled with product detection by mass spectrometry. The reduction procedure was performed under H_2 (10% in helium) at a rate of 10 °C min^{-1}. The reaction was conducted at a temperature of 200 °C and pressurized to 20 bar with a flow of CO_2/H_2 in a 1:4 ratio, and it was followed for 3 h. During the reaction, all XANES were recorded at 200 °C. For steady-state EXAFS, the cell was cooled to room temperature for data collection, and nine scans were averaged to improve the signal-to-noise ratio. The Demeter software package, version 0.9.26, was used for data normalization and EXAFS fitting. For EXAFS modeling, the scattering paths were generated using CIF files from the Inorganic Crystal Structures Database (ICSD). The Re (ICSD-650068) and ReO_2 (ICSD-24060) files were used to create metallic Re−Re and Re−O paths, respectively.

The H_2 temperature-programmed reduction (H_2-TPR) analyses were performed using an AutoChem II 2920 instrument (Micromeritics). A quartz reactor was loaded with 80 mg of catalyst and pretreated at 200 °C under a flow rate of 30 mL min^{-1} of He. The sample was then cooled to room temperature and exposed to a 30 mL min^{-1} flow of 10% H_2/N_2 for 20 min, followed by heating to 850 °C at a rate of 10 °C min^{-1}. The hydrogen consumption was determined by analysis of the effluent gases using a thermal conductivity detector (TCD). Transmission electron microscopy images were acquired on a JEOL 2100 F or a FEI Talos F200X microscope, operating at an acceleration voltage of 200 kV with a field-emission gun, or FEI Titan Cubed Themis, operating at 300 kV. The images were acquired using conventional TEM and Scanning TEM (STEM) to enhance the contrast between Re and TiO_2. The catalyst was dispersed in water, and dripped onto an ultrathin carbon film-coated Cu grid (Ted Pella). STEM images were acquired using a high-angle annular dark field detector. A histogram of the nanoparticle size distribution was evaluated through these images by measuring particles and fitting the histogram with a log-normal function.

Catalytic Tests. The supercritical flow reaction system was built in-house and is described elsewhere.[28] Briefly, a syringe
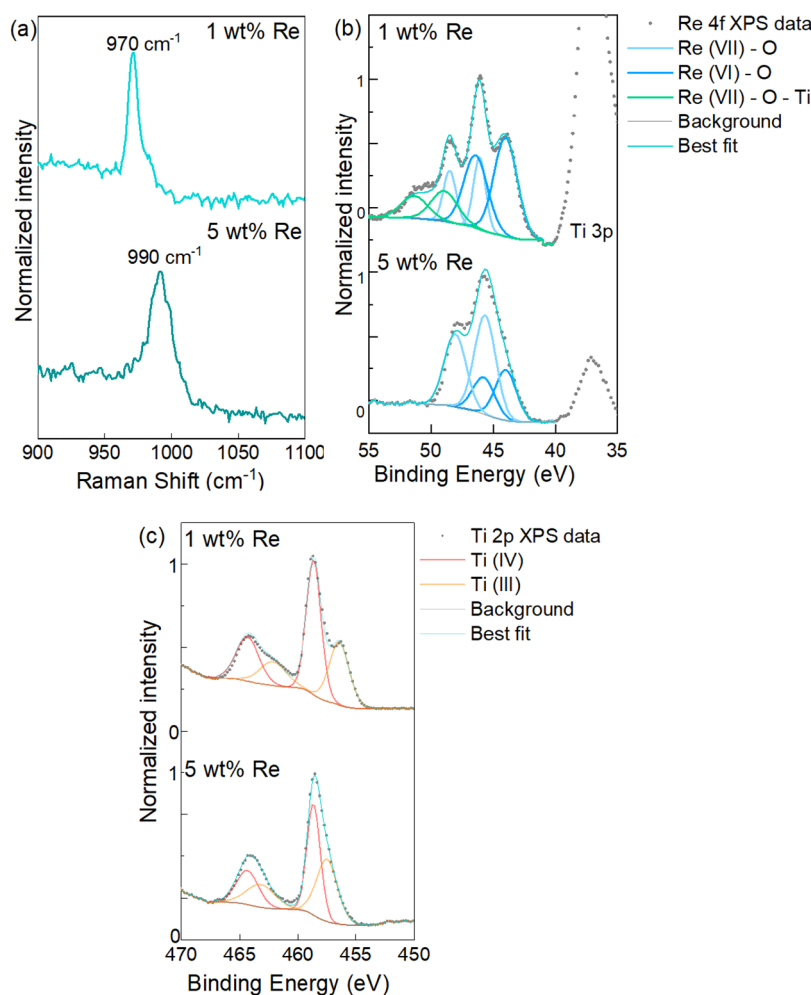
Figure 1. (a) Raman spectra and (b) XPS of rhenium standards and rhenium catalysts Re/TiO_2 with 5 and 1 wt % Re as prepared in the Re 4f region and (c) Ti 2p region.

pump Isco model 500D pressurized the gas mixture of CO_2 and H_2 and controlled the flow rate into a fixed-bed reactor (stainless steel tubing, 1/4″, ID: 3.175 mm) packed with 290 mg of the Re/TiO_2 heterogeneous catalyst. A six-way sampling valve (Rheodyne 7000L) was used to collect samples and evaluate CO_2 hydrogenation under pressure, and a spring-loaded piston backpressure valve (CITUA, Brazil) controlled the pressure. Analyses of reaction products were performed in a Shimadzu QP2010 gas chromatographer equipped with TCD and MS. CH_4, CO, and CO2 were analyzed with a Carboxen 1010 column on TCD, and CH_3OH was analyzed with a Stabilwax column by MS. The high-pressure flow reactions were followed for 6 h. After 1 h of reaction, the product concentration values obtained by GC analyses stabilized, and these were used in the calculation of the conversion, selectivity, and space-time yield values presented here.

Thermodynamic Equilibrium. The equilibrium composition of the reaction system was determined using the Gibbs free energy minimization method. At equilibrium, the system's total Gibbs free energy (G) reaches its minimum, with its differential equaling zero.[41,42] Based on this theory, the Aspen Plus software features the RGibbs module, which calculates the composition at equilibrium using only pressure and temperature as input variables, without requiring stochiometric or kinetic information. Version 8.8 of Aspen Plus was utilized to calculate conversion and product selectivities. From the

RGibbs input and output compositions, the CO_2 conversion was calculated using eq 1, the H_2 conversion using eq 2, and the selectivity using eq 3.

$$X_{CO_2} = \left[\frac{(F_{in,CO_2} - F_{out,CO_2})}{F_{in,CO_2}}\right] \cdot 100 \tag{1}$$

$$X_{H_2} = \left[\frac{(F_{in,H_2} - F_{out,H_2})}{F_{in,H_2}}\right] \cdot 100 \tag{2}$$

$$S_i = \left[\frac{\lambda \cdot F_{out,i}}{F_{in,CO_2} - F_{out,CO_2}}\right] \cdot 100 \tag{3}$$

X_i: i Conversion; $F_{in,i}$: Molar flow rate of i at inlet; $F_{out,i}$: Molar flow rate of i at outlet; S_i: i Selectivity; λ: number of carbon atoms in species i.

The SRK equation of state, as modified by Mathias,[43] was employed in this study, utilizing pure and binary interaction parameters as detailed by Bennekom et al.[44] Based on the experimentally proposed reaction conditions, the components selected for the simulation were H_2, CO_2, CO, CH_3OH, CH_4, and H_2O. Following an initial run at 200 °C and 100 bar, a sensitivity analysis was conducted by varying the temperature (150−300 °C), pressure (1, 20, 40, 60, 80, 100, and 120 bar),

and CO_2/H_2 ratio (1:1, 1:2, 1:3, 1:4, 1:5, and 1:10). Further details are provided in Supporting Information.

Theoretical Models and Methodology. Bulk anatase TiO_2 forms a tetragonal lattice with the space group $I4_1/amd$, and the experimental lattice constants are $a = b = 3.776$ Å and $c = 9.486$ Å. We built a periodic slab with four layers for (101) facets. A four-layer 4×2 supercell was used. The $TiO_2(101)$ facets are chosen because anatase $TiO_2(101)$ facets are the dominant facets in the experimental sample. The bottom two layers of Ti and O are fixed, while the top two are relaxed during the calculation. The vacuum thickness was optimized to be 20 Å.

All calculations were carried out within the DFT formalism in the Vienna Ab Initio Simulation Package (VASP) electronic structure code[45] using the PBE exchange-correlation functional[46] and 450 eV plane-wave cutoff. γ-centered k-point meshes of $3 \times 3 \times 1$ were used. The PAW method was used to describe the effect of core electrons.[47] All structures were relaxed until the forces acting on each atom were smaller than 1×10^{-4} eV Å^{-1}. Transition states along the reaction pathways are searched by the Climbing Image Nudged Elastic Band (CI-NEB) approach.[48,49] Adsorption energies have been calculated using the formula: $E_{ads} = E_{adsorbate+slab}^{DFT} - E_{slab}^{DFT} - \sum_i \alpha_i E_{i,gas}^{DFT}$. The free energies of species were calculated as: $G = E_{DFT} + E_{ZPE} - T \cdot S$, where E_{ZPE} and $T \cdot S$ of adsorbed species were calculated by vibration analysis.

RESULTS AND DISCUSSION

Effect of Rhenium wt % and Prereduction under H_2 on Rhenium Species and Catalytic Activity. The Re/TiO_2 catalysts were synthesized through wet impregnation of commercially available TiO_2 (P25) with ReO_4^-, derived from an aqueous solution of Re_2O_7, followed by drying in air at 120 °C, and a finally a thermal treatment under H_2 at 250 or 500 °C to produce the metallic rhenium clusters, which is performed in situ in the reactor. However, not all characterization techniques were available with in situ heating under H_2. The analysis of Re/TiO_2 with ex situ prereduction could lead to poor interpretation of the results, as rhenium nanoclusters are known to be very easily reoxidized when exposed to air, even if at ambient temperature.[50−52] Therefore, the as prepared Re/TiO_2 catalysts were also characterized prior to the reduction, when rhenium oxide species were still present. The understanding of the nanostructure of the rhenium oxides in the as prepared catalysts can aid in the interpretation of the characterizations of in situ reduced metallic Re/TiO_2. The Raman spectra of the as-prepared Re/TiO_2 catalysts were measured (Figure 1a) and compared to ReO_2, ReO_3, and NH_4ReO_7 as standards (Figure S1). Raman measurements were obtained ex situ with samples exposed to air, with no prereduction step. As seen on Figure 1a, the sample with 5 wt % Re has a peak similar to that from ReO_3 around 990 cm^{-1}, whereas the catalyst with 1 wt % Re has a peak closer to the NH_4ReO_4 standard at 970 cm^{-1}, indicating that the as-prepared catalysts have slightly different configurations of supported rhenium oxides.[53] The presence of peaks in the 970−990 cm^{-1} region of the Raman spectra of Re/TiO_2 materials is consistent with dioxo or trioxo rhenium species, with multiple Re=O terminal bonds.[54] Vuurman et al.[55] also found a 970 cm^{-1} Raman band for a Re_2O_7/TiO_2 as-prepared catalyst, which moved to 1005 cm^{-1} after in situ dehydration by thermal treatment at 450 °C under oxygen for 1 h.

The Raman band at 970 cm^{-1} matches that of the symmetric stretching mode of a tetrahedral ReO_4^- in aqueous solution,[56,57] which is the species present when the aqueous impregnation of TiO_2 is performed with Re_2O_7 as a rhenium precursor, suggesting that rhenium oxide maintains a geometry similar to aqueous $Re_2O_7^-$ when impregnated on TiO_2. The higher frequency peak at 990 cm^{-1} relates to symmetric stretching of a terminal Re=O species on adsorbed Re− and can also be observed on ReO_3 as a surface defect of this oxide.[58] A shift to higher frequencies of Raman peaks on supported rhenium catalysts has been associated with dehydration of the surface, when comparing the same sample before and after calcination at 450 °C.[55,56] This could indicate that the 5 wt % Re catalyst contains fewer surface hydroxyls, which is consistent with surface −OH groups serving as anchor sites for Re species upon catalyst synthesis.[59,60] Raman spectra at their full scale from 200 to 1100 cm^{-1} of these samples can be seen in Figure S1.

XPS analyses of the as-prepared catalysts (Figure 1b and Table 1) suggest that the surface of as-prepared Re/TiO_2

Table 1. XPS Data of the Re $4f_{7/2}$ Region on As-Prepared Re/TiO_2 Catalysts

	binding energy (eV)	atom %
5 wt % Re/TiO_2		
Re(VI)−O	44.0	34
Re(VII)−O	45.7	66
1 wt % Re/TiO_2		
Re(VI)−O	44.0	58
Re(VII)−O	46.1	22
Re−O−Ti $\delta+$ (~VII)	48.9	20

presents both Re(VII) and Re(VI), even though the aqueous impregnation was performed with ReO_4^- which is a Re(VII) species. At this point, no chemical reduction process had been performed. The presence of Re(VI) could be due to exposure to X-rays during XPS, which causes the reduction of surface rhenium species.[61,62] The 5 wt % Re/TiO_2 sample contains 66 atom % of Re(VII) at a binding energy of 45.7 eV for the Re $4f_{7/2}$ component and 34 at% of Re(VI) at a binding energy of 44.0 eV. The surface of the 1 wt % sample contains 58 atom % of Re(VI) at 44.0 eV and 22 atom % of Re(VII) at 46.1 eV. These results are in agreement with the XPS analyses reported for similar Re/TiO_2 samples.[26,63,64] An additional component appears in the Re $4f_{7/2}$ XPS region of 1 wt % Re/TiO_2 at 48.9 eV, which is over 2 eV higher than the energy levels reported for Re(VII) in rhenium oxide species,[65] and accounts for 20% of surface rhenium. Therefore, the presence of a Re $4f_{7/2}$ peak at 48.9 eV may be related to a Re(VII) species with strong interaction with the TiO_2 support in a Re−O−Ti bond with charge transfer from rhenium to titanium,[31,66] a phenomenon also reported on by Shimizu et al, who demonstrated through experimental and computational approaches that TiO_2 can accept electrons from rhenium into its conduction band, therefore leading to a strong metal−support interaction.[67] XPS analyses of the as-prepared catalysts in the Ti 2p region (Figure 1c) show a lower binding energy for Ti(III) $2p_{3/2}$ on 1 wt % Re/TiO_2 (456.4 eV) than on 5 wt % Re/TiO_2 (457.4 eV), which agrees with the presence of a strong interaction with the support through a Re−O−Ti bond on the sample with lower metal loading.
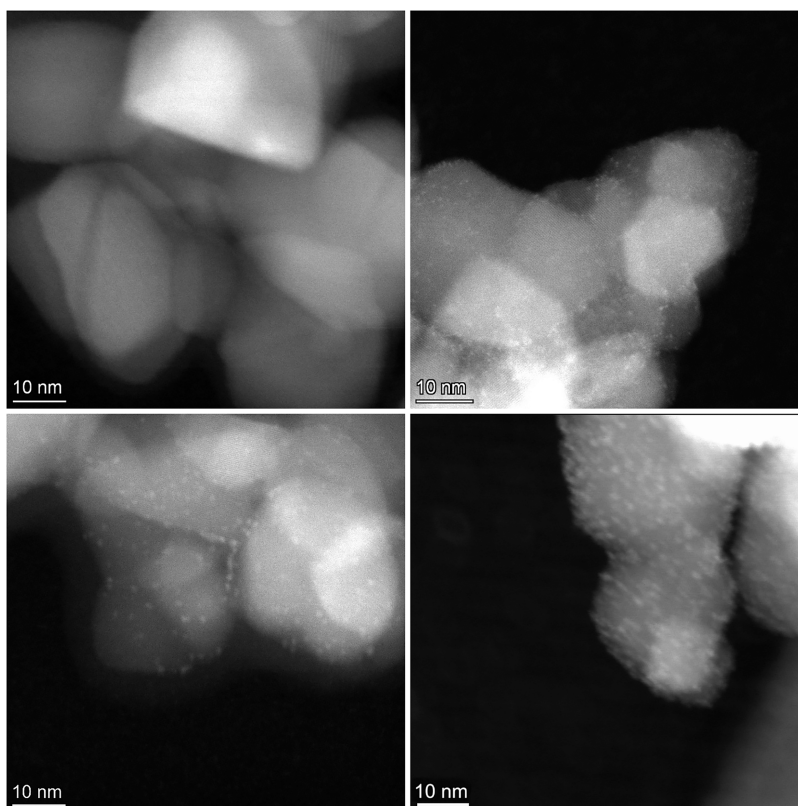
Figure 2. HR-STEM images of as-prepared 1 wt % Re/TiO_2 (top left), 1 wt % reduced at 500 °C (top right), as-prepared 5 wt % Re/TiO_2 (bottom left) and 5 wt % reduced at 500 °C (bottom right).

The XRD pattern of the as-prepared Re/TiO_2 catalysts only show peaks due to the TiO_2 anatase and rutile phases of TiO_2, consistent with the TiO_2 P25 used as support, which is a mixture of 80% anatase and 20% rutile. The rhenium oxide species may be too small in size, amorphous, or too low in concentration to be detected by XRD. The 5 wt % Re/TiO_2 sample prereduced at 500 °C was the only one to show metallic rhenium peaks at $2\theta = 37.5°$ ($1\bar{1}0$), 40.3° (002), 42.8° ($1\bar{1}1$), and 56.3° ($1\bar{1}2$), which correspond to the hexagonal close packed structure of rhenium (ICSD 650068). The XRD data are shown in Figure S2. The HR-STEM analysis of the Re/TiO_2 catalysts is displayed in Figure 2. The as-prepared 1 wt % Re/TiO_2 catalyst had no visible rhenium nanoclusters. When reduced at 500 °C, the 1 wt % sample presented subnanometric clusters averaging 0.5 ± 0.2 nm. Meanwhile, on 1 wt % Re/TiO_2 reduced at a lower temperature of 250 °C, some subnanometric clusters of around 0.2 nm were visible; however, their population was not statistically significant (Figure S3). The 5 wt % Re/TiO_2 catalyst revealed a uniform distribution of rhenium nanoclusters on the TiO_2 crystals, with an average size of 1.0 ± 0.2 nm, both on the as-prepared catalyst and when reduced at 250 °C,[28] with a slight increase to 1.1 ± 0.3 nm on the reduced catalyst at 500 °C under H_2. The size distribution histograms and fitted curves are shown in Figure S4.

To further elucidate the structure of Re/TiO_2, a series of XAS experiments were conducted on as-prepared 1 and 5 wt % Re/TiO_2 (after aqueous impregnation of Re_2O_7 on TiO_2 and air-dried at 120 °C), which were then reduced *in situ* under H_2 (diluted to 5% in He) from room temperature up to 500 °C. As seen on Re L_3-edge XANES spectra collected at room temperature (Figure 3a), the spectra of Re/TiO_2 vary with the weight percentage of rhenium. The absorption edge energy, defined as the maximum of the first derivative of μE plotted against energy, is very similar for the two as-prepared catalysts of different rhenium loading (Figure S5). After reduction at 500 °C, the white line for each catalyst is substantially less intense, and the absorption edge is shifted to a lower value, both of which are consistent with the reduction of rhenium.

To relate the absorption edge position to the average Re oxidation state, the XAS of Re_2O_7, ReO_3, ReO_2, and metallic Re were obtained (Figure S6).[68] The data suggest that both as-prepared 1 and 5 wt % Re/TiO_2 catalysts have an average oxidation state of rhenium close to +7, and close to zero after *in situ* reduction at 500 °C. A linear regression of the E_0 values of the rhenium standards (Figure S7) reveals that both 1 and 5 wt % Re/TiO_2 catalysts have an average oxidation state of +1.2 after 1 h reduction at 500 °C under H_2, cooling under He, and measured *in situ* at room temperature. Due to its large size and oxophilicity, rhenium only forms stable oxides of higher oxidation state, with ReO_2 (Re^{4+}) as the oxide of lowest rhenium oxidation state. „ReO" or „Re_2O" only exists on the surface of metallic rhenium.[65,69] Therefore, the XANES of the reduced Re/TiO_2 catalysts suggest that their active sites are composed of metallic rhenium nanoclusters in close interaction with oxygen atoms from the TiO_2 support.

XANES of Re L_3-edge during temperature-programmed-reduction in 5% H_2/He (H_2-TPR) of the Re/TiO_2 catalysts were performed to understand any differences in the reduction behavior of the two catalysts (Figure 3b,c). The main reduction event occurs in the 150−250 °C range for both catalysts, with the reduction of the 1 wt % Re starting at a slightly lower temperature, and over a larger temperature range. These results are in good agreement with the laboratory
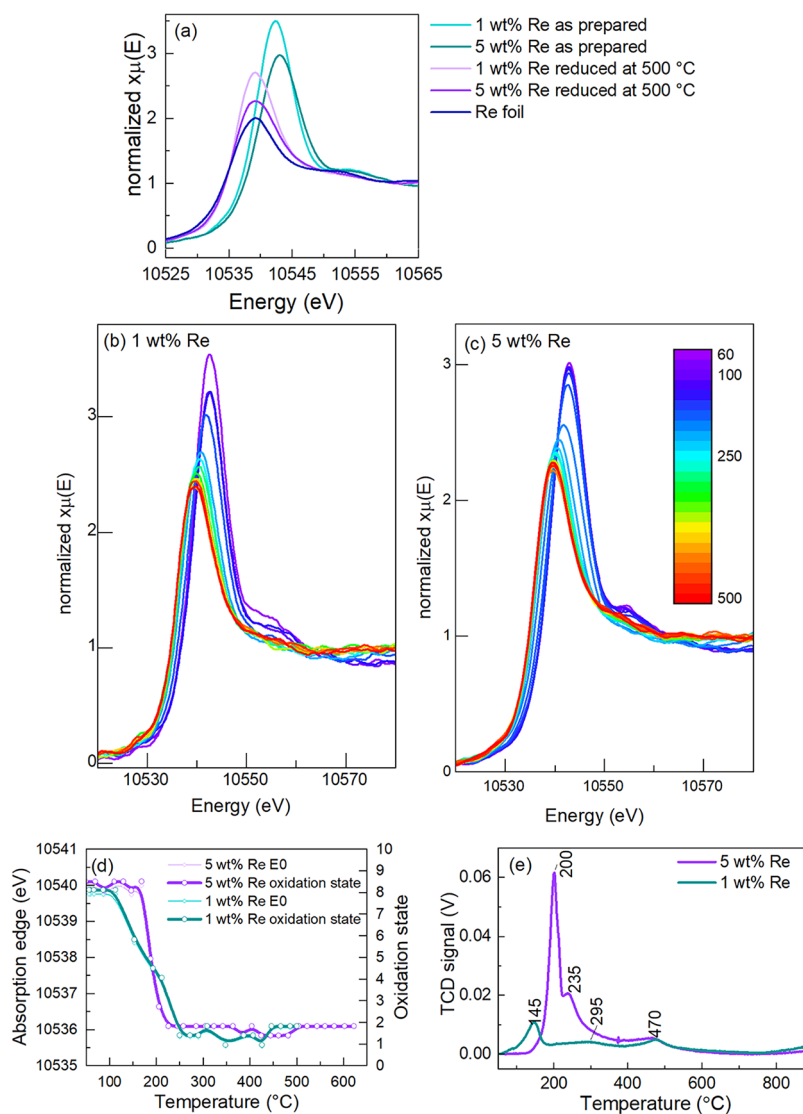
Figure 3. (a) Re L$_3$-edge XANES of Re/TiO$_2$ samples obtained at room temperature, (b, c) Re L$_3$-edge XANES of 1 and 5 wt % Re/TiO$_2$ catalysts measured during *in situ* H$_2$-TPR, (d) absorption edge energy and oxidation state of rhenium in Re/TiO$_2$ samples during reduction with H$_2$, and (e) TCD signal of H$_2$ consumption.
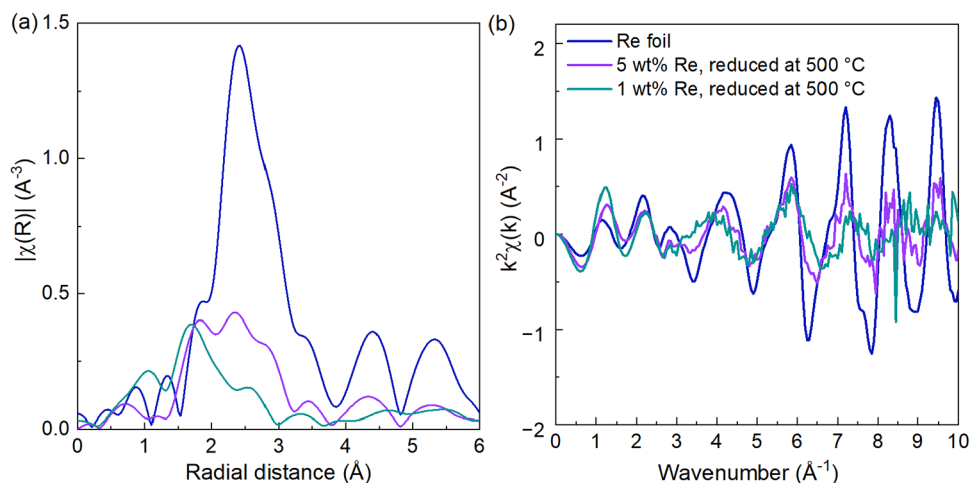
Figure 4. (a) Magnitude of the FT (*k* range 3−10.5 Å^{-1}) and (b) *k*$_2$-weighted Re L$_3$-edge EXAFS in *k* space of Re/TiO$_2$ of 5 or 1 wt % rhenium with *in situ* reduction under H$_2$, compared to metallic Re.

Table 2. EXAFS Fitted Parameters for 5 wt % Re/TiO$_2$ (k = 3–10.5 Å^{-1}; k Weight = 1, 2, 3)

5 wt % Re/TiO$_2$	path	CN	R (Å)	σ (10^{-3} Å^2)	E$_0$ (eV)
as prepared	Re–O	4.6 ± 0.7	1.71 ± 0.01	0.5 ± 1.3	2.4 ± 2.7
	Re–O	1.0 ± 0.6	2.10 ± 0.03	0.5 ± 1.3	2.4 ± 2.7
reduced at 250 °C	Re–Re	2.3 ± 0.5	2.73 ± 0.02	6.6 ± 1.3	5 ± 2
	Re–O	1.1 ± 0.2	2.08 ± 0.02	1.4 ± 2.3	14 ± 2
reduced at 500 °C	Re–Re	5.4 ± 1.1	2.76 ± 0.01	6.6 ± 1.3	5 ± 2
	Re–O	1.4 ± 0.4	2.11 ± 0.03	5.8 ± 2.8	14 ± 2
reduced at 250 °C–after reaction	Re–Re	2.7 ± 0.7	2.73 ± 0.02	6.6 ± 1.3	5 ± 2
	Re–O	1.2 ± 0.3	2.11 ± 0.02	1.4 ± 2.3	14 ± 2
reduced at 500 °C–after reaction	Re–Re	6.8 ± 1.1	2.76 ± 0.01	6.6 ± 1.3	5 ± 2
	Re–O	2.3 ± 0.5	2.12 ± 0.02	5.8 ± 2.8	14 ± 2
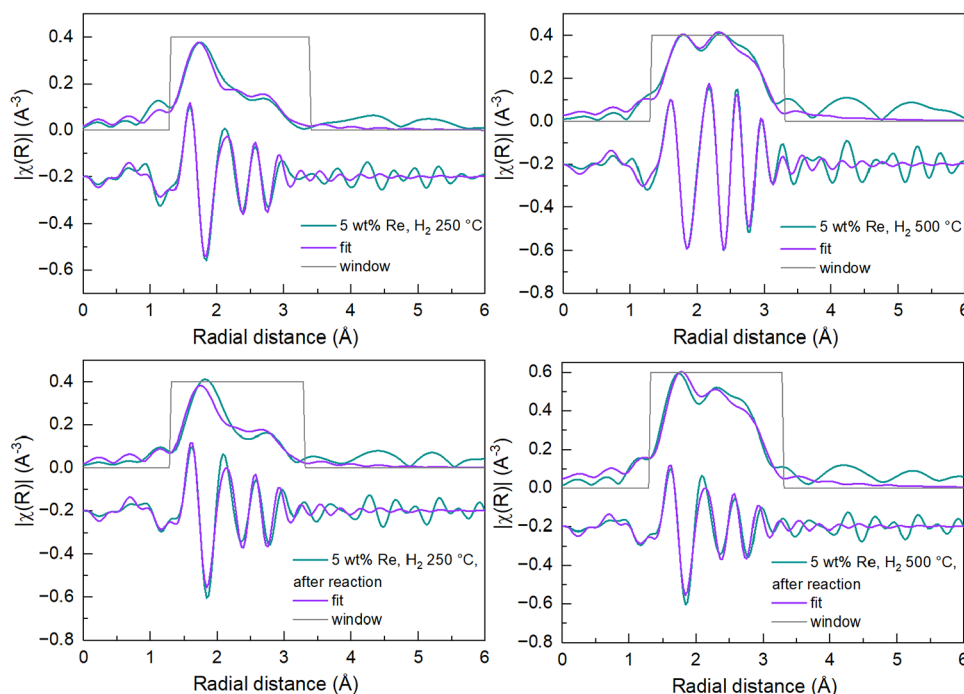
Figure 5. Best fit EXAFS models of Re/TiO$_2$ samples. Magnitude (upper) and imaginary (lower) of the FT plotted in each panel. All data recorded at room temperature. Top left 5 wt % Re after 250 °C reduction. Top right 5 wt % Re after 500 °C reduction. Bottom left 5 wt % Re reduced at 250 °C after reaction. Bottom right 5 wt % Re reduced at 500 °C after reaction. Fit range 1.2 to 3.4 Å. The EXAFS fit in k-space is shown in SI.

H$_2$-TPR with H$_2$ consumption measured by TCD (Figure 3e). The higher dispersion of rhenium clusters on 1 wt % Re/TiO$_2$ can explain the lower reduction temperature at 145 °C, as more Re atoms are exposed to H$_2$ in a smaller particle. The XPS analyses (Figure 1b) revealed that 1 wt % Re/TiO$_2$ also contains rhenium species with a stronger interaction with the TiO$_2$ support. These would be more resistant to reduction, which could explain the broader TPR peaks and the slower decrease in oxidation state with temperature.

In order to gather information about the rhenium species present during the catalysis, Re L$_3$-edge XANES was also obtained *in operando* for the hydrogenation of CO$_2$ over the 5 wt % Re/TiO$_2$ catalyst, prereduced at 500 °C at 20 bar. The experimental conditions at the beamline were slightly different than those of the catalytic reaction evaluations, as the reaction gases were at lower pressure and diluted in helium. In all cases, there are only minor differences in the Re L$_3$-edge XANES between those of the reduced catalyst and the operando spectrum (Figure S8).

The Re L$_3$-edge EXAFS data of the catalysts reduced *in situ* at 500 °C, plotted as the magnitude of the Fourier transform

(Figure 4), reveal that 5 wt % Re/TiO$_2$ has a more significant contribution of metallic rhenium species than 1 wt % Re/TiO$_2$, as indicated by the presence of a peak at 2.3 Å. This finding suggests that the catalyst with a higher percentage of rhenium contains more reduced rhenium species, despite the similarity in absorption edge energy, which is compatible with small metallic clusters interacting with oxygen atoms from TiO$_2$. This suggests that 1 and 5 wt % Re/TiO$_2$ have similar rhenium average oxidation states but exhibit an increase in cluster size with increasing rhenium amount, as reported for similar samples.[70,71] The best fit EXAFS data for the 5 wt % Re/TiO$_2$ is provided in Table 2 and Figure 5. (The respective k-space plots are given in Figure S9). The first Re–Re scattering path coordination numbers obtained for the 5 wt % catalysts prereduced at 250 or 500 °C were 2.3 ± 0.5 and 5.4 ± 1.1, respectively. The larger coordination number found for the sample reduced at a higher temperature indicates a larger Re cluster, which could also explain the lower white line intensity observed in the Re L$_3$-edge XANES of Re/TiO$_2$ reduced at the higher temperature, even though these samples presented the same absorption edge energy (Figure S10).[71] Both samples
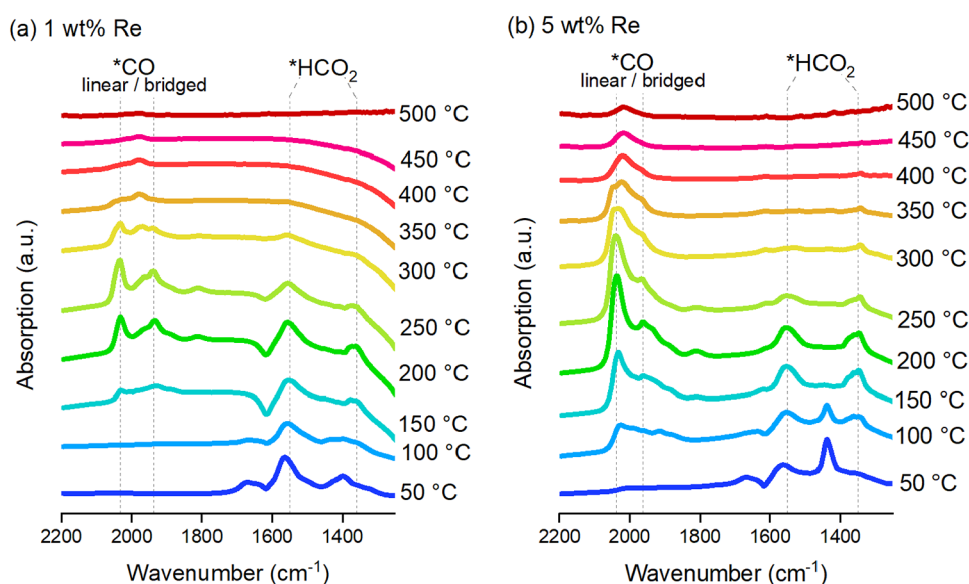
Figure 6. Diffuse reflectance infrared Fourier-transformed spectroscopy (DRIFTS) of Re/TiO_2 with (a) 1 wt % of Re and (b) 5 wt % of Re prereduced under H_2 at 500 °C and exposed to a mixture of CO_2 and H_2 (ratio of 1:4) at ambient pressure and various temperatures.

Table 3. Effect of Rhenium wt % and Temperatures of Pre-Reduction and Reaction on the High-Pressure Hydrogenation of CO_2 over Re/TiO_2 in a Fixed-Bed Reactor Packed 290 mg of Catalyst, P = 100 bar, CO_2/H_2 = 1:4, GHSV = 10,000 mL·g_{cat}^{-1}·h^{-1}, Time on Stream = 6 h

| Re wt %	T prereduction (°C)	T reaction (°C)	CH_3OH STY[a]	selectivity (%)			CO_2 conversion (%)
				CH_3OH	CO	CH_4	
1	250	200	15	80	<1	20	7
1	250	250	28	46	<1	53	21
1	500	200	55	99	<1	<1	19
1	500	250	65	97	1	1	23
5	250	150	2	97	<1	3	4
5	250	200	8	98	<1	2	18
5	250	250	13	65	<1	35	40
5	500	250	16	74	1	25	40
5	500	200	18	97	<1	3	33

[a]Space time yield (STY) calculated as grams of CH_3OH produced per gram of Re per hour.

presented a slight increase in average Re−Re coordination number after 5 h of reaction (200 °C and 20 bar), where a CN of 2.7 ± 0.7 (from 2.3 ± 0.5) was found for postreaction Re/TiO_2 prereduced at 250 °C and 6.8 ± 1.1 (from 5.4 ± 1.1) for the sample prereduced at 500 °C. Unfortunately, the XAS data quality of the 1 wt % Re/TiO_2 sample did not allow for a reliable EXAFS modeling due to the poor signal quality. Comparatively, Toyao et al.[26] found a Re−Re CN of 3.4 for a 5 wt % Re/TiO_2 catalyst prereduced also at 500 °C, but for a shorter time of 0.5 h as opposed to the 1-h reduction time employed in this study, and with a previous calcination step at 500 °C for 3 h in air. Yang et al.[70] found an even lower Re−Re coordination number of 1.8 ± 0.4 for a similar 5 wt % Re/TiO_2 sample prereduced at the same temperature of 500 °C for 0.5 h, but synthesized through the strong electrostatic adsorption impregnation method, which points to a significant effect of small changes in synthesis methodology on the nanostructure of the catalytic active site.

The DRIFTS analyses of the 1 and 5 wt % Re/TiO_2 catalysts (Figure 6) in a flow of CO_2/H_2 (1:4 ratio) indicate the species adsorbed on the catalytic surface under a flow of CO_2 and H_2 diluted in argon at atmospheric pressure. Both samples present

vibrational bands around 1350 and 1550 cm^{-1}, which are almost entirely absent at 300 °C. These bands can be assigned as bidentate formate on TiO_2.[31] Both samples also present bands around 2000−1800 cm^{-1} that can be attributed to adsorbed CO species.[31,70,72] These adsorbed CO bands appear at 150 °C and increase in intensity with temperature up to 250 °C and begin to decrease at 300 °C, which indicates that these species were formed under reaction conditions.

The sample with 5 wt % Re has a higher intensity of linearly adsorbed CO on the edge sites at 2038 cm^{-1} and lower intensity bands at 1963, 1881, and 1808 cm^{-1}, which can be ascribed to bridged-CO adsorbed on perimeter Re−Ti sites or on two Re atoms.[70] The 1 wt % sample has bands of similar intensity for linear CO at 2034 cm^{-1} and bands at 1968, 1938, and 1810 cm^{-1}. The higher intensity of linearly adsorbed CO on the 5 wt % Re sample is expected due to the higher metal content, and thus higher particle size, whereas the 1 wt % Re sample may have more surface defects, which would facilitate the bridged configuration of adsorbed CO species.[70,73,74] The IR bands between 2000−1800 cm^{-1} include vibrations from rhenium hydrides,[75,76] rhenium carbonyls and bidentate
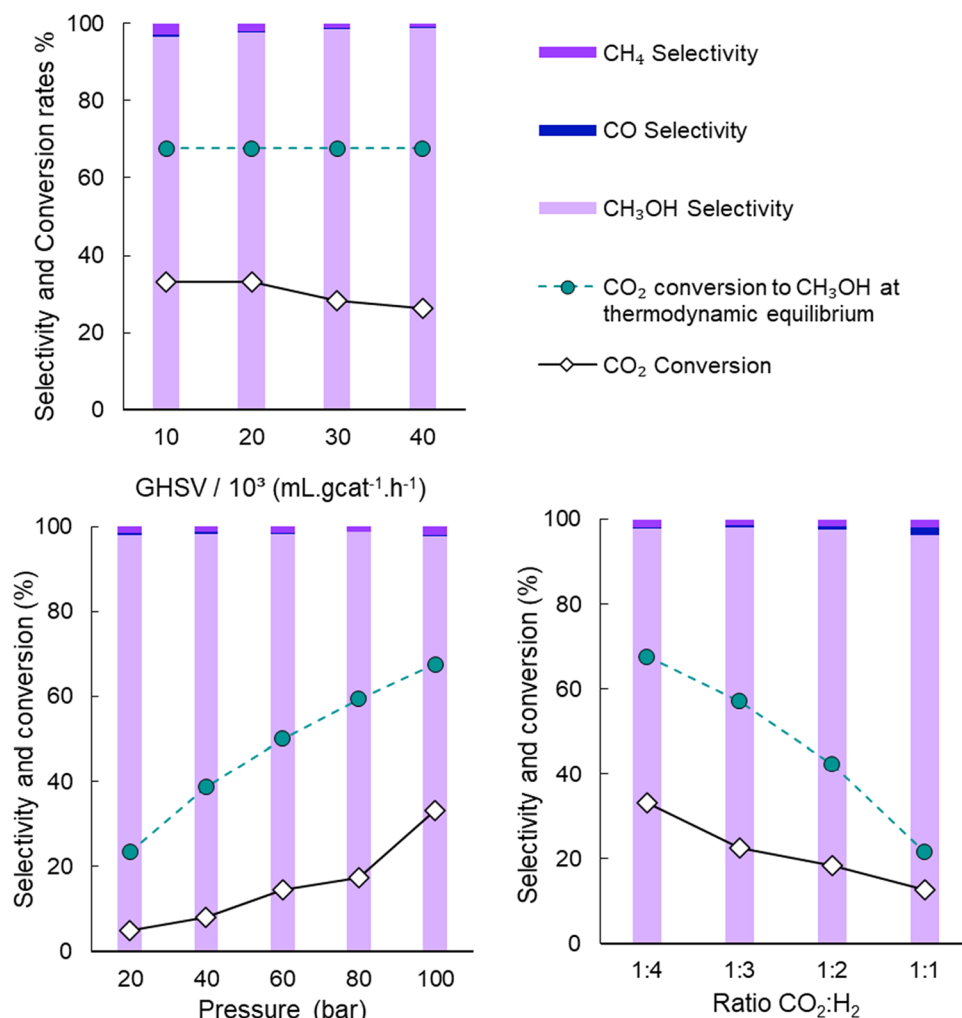
Figure 7. High pressure hydrogenation of CO_2 over 5 wt % Re/TiO_2. Reaction conditions (unless otherwise specified): fixed-bed reactor packed 290 mg of 5 wt % Re/TiO_2 prereduced at 500 °C, P = 100 bar, CO_2/H_2 = 1:4, T = 200 °C; GHSV = 20,000 $mL·g_{cat}^{-1}·h^{-1}$. Thermodynamic equilibrium conversion considered only CO_2 to CH_3OH.

adsorbed CO,[31] which are difficult to distinguish due to their superpositions.

Table 3 presents data on the catalytic activity in the high-pressure hydrogenation of CO_2 over Re/TiO_2 with varying reduction temperatures and rhenium amounts. Generally, an increase in the reaction temperatures from 200 to 250 °C was detrimental to CH_3OH selectivity, as more CH_4 is formed at higher temperatures in this range, due to the kinetic limitations of the methanation reaction.[6] At 150 °C, the selectivity is high, but the conversion of CO_2 is low, even at 100 bar, as we have previously reported.[28] Performing the reduction of the Re/TiO_2 catalyst with 5 wt % Re at the higher temperature of 500 °C instead of 250 °C improves methanol productivity at both reaction temperatures of 200 and 250 °C. However, CH_4 is still a problematic side product when the reaction is performed at 250 °C.

Meanwhile, the decrease in amount of rhenium from 5 to 1 wt % had a positive effect on methanol selectivity at both reaction temperatures, although the conversion of CO_2 decreased. For 1 wt % Re/TiO_2 reduced at 500 °C, a selectivity of 99% methanol at 19% CO_2 conversion was achieved at 200 °C. At the same reaction conditions for 5 wt % Re/TiO_2, a selectivity of 97% methanol at a CO_2 conversion of 33% was obtained. Although conversion was higher with the

catalyst with 5 wt % Re, the methanol space-time yield (STY) per gram of rhenium was higher for the catalyst with only 1 wt % (55 against 18 $g_{CH_3OH}·g_{Re}^{-1}·h^{-1}$).

Influence of Reaction Conditions for the High-Pressure Hydrogenation of CO_2 to Methanol. The reaction conditions, including space velocities, pressures, and CO_2/H_2 ratios, were evaluated for their impact on CO2 conversion and methanol selectivity. The hydrogenation of CO_2 was performed at 200 °C in a stainless steel fixed-bed flow reactor packed with Re/TiO_2 catalysts reduced at 500 °C (Figure 7 and Table 4). The CO_2 conversion was affected by all of the evaluated variables. A higher gas hourly space velocity (GHSV) of 40,000 $mL·g_{cat}^{-1}·h^{-1}$ led to a conversion of 26% while a lower one of 10,000 $mL·g_{cat}^{-1}·h^{-1}$ gave a conversion of 33%, which is expected since higher space velocities give shorter contact times on the catalyst. Higher pressures significantly increased CO_2 conversion, which was 5% at 20 bar and 33% at 100 bar. Thermodynamically, increasing pressures positively affect methanol formation from CO_2.[28]

Ratios of CO_2/H_2 with excess hydrogen, such as 1:4, gave high CO_2 conversion. While the catalytic performances at higher space velocities and CO_2-rich reactant mixtures show slightly lower conversions, these are still interesting from an

Table 4. Catalytic Performance of Re/TiO$_2$ on the High-Pressure Hydrogenation of CO$_2$ to CH$_3$OH^{ab}^{,c}

| Re (wt %)	T prereduction (°C)	T reaction (°C)	pressure (bar)	CO$_2$/H$_2$	CH$_3$OH STY^c	CH$_3$OH	CO	CH$_4$	conversion of CO$_2$	GHSV^c (10^3)
						selectivity				
1	250	200	100	1:4	15	80	<1	20	7	10
1	250	250	100	1:4	28	46	<1	53	21	10
1	500	200	100	1:4	55	99	<1	<1	19	10
1	500	250	100	1:4	65	97	1	1	23	10
5	250	150	100	1:4	2	97	<1	3	4	10
5	250	200	100	1:4	8	98	<1	2	18	10
5	250	250	100	1:4	13	65	<1	35	40	10
5	250	250	100	1:4	30	89	1	11	29	20
5	250	250	100	1:4	49	94	1	5	22	40
5	500	250	100	1:4	16	74	1	25	40	10
5	500	200	100	1:4	18	97	<1	3	33	10
5	500	200	100	1:4	37	98	<1	2	33	20
5	500	200	100	1:4	48	99	<1	1	28	30
5	500	200	100	1:4	59	99	<1	1	26	40
5	500	200	80	1:4	20	99	<1	1	17	20
5	500	200	60	1:4	16	98	<1	1	14	20
5	500	200	40	1:4	9	98	1	1	8	20
5	500	200	20	1:4	6	98	1	1	5	20
5	500	200	100	1:3	32	98	<1	1	22	20
5	500	200	100	1:2	35	98	1	2	18	20
5	500	200	100	1:1	36	96	2	2	13	20

^{a}Reaction conditions: fixed bed reactor packed with 290 mg of Re/TiO$_2$. ^{b}Space time yield (STY) calculated as grams of CH$_3$OH produced per gram of Re per hour. ^{c}Gas hourly space velocity (GHSV) calculated as mL·g$_{cat}^{-1}$·h^{-1}
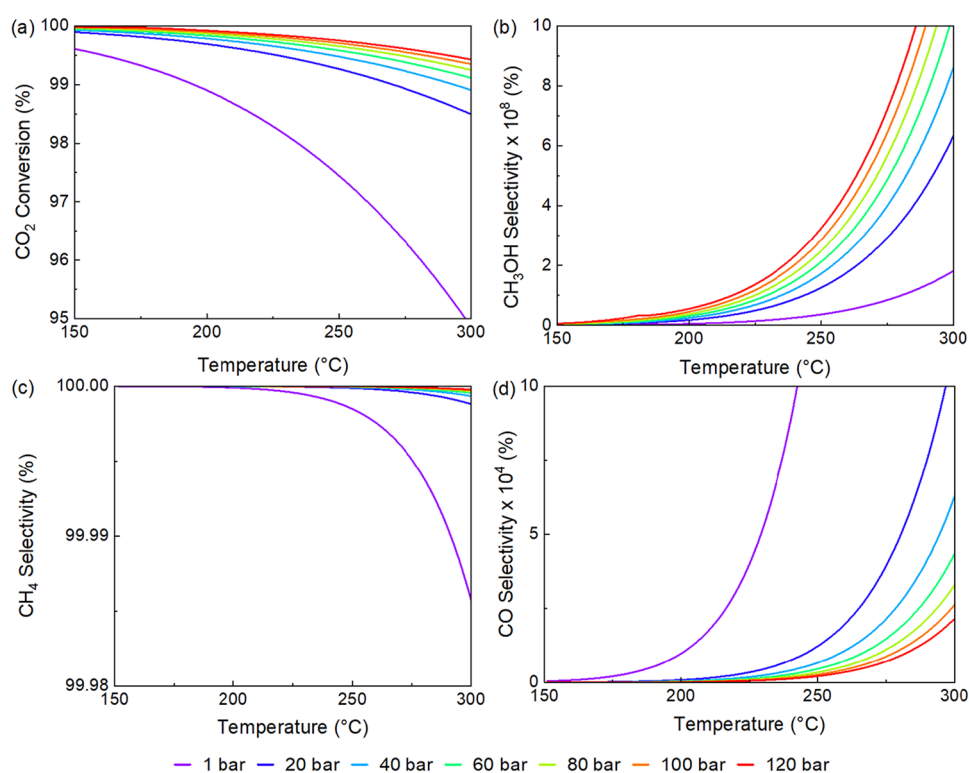
Figure 8. Thermodynamic equilibrium simulated (a) CO$_2$ conversion, (b) CH$_3$OH selectivity, (c) CH$_4$ selectivity and (d) CO selectivity.

industrial perspective, as they allow for a greater amount of CO$_2$ to be processed at a given time. At pressures between 20 and 100 bar at T = 200 °C, none of the aforementioned variables had a significant impact on reaction selectivity, attesting to the suitability of Re/TiO$_2$ as an effective catalyst for CO$_2$ hydrogenation to CH$_3$OH. Remarkably, the methanol

selectivity was still high (96%) even at unfavorable conditions such as CO$_2$/H$_2$ = 1:1 (Figure 7). Methanol selectivity was also stable at 98−99% through the range of higher pressures of 20−100 bar, and only varies from 97 to 99% when increasing GHSV from 10,000 to 40,000 mL·g$_{cat}^{-1}$·h^{-1}. Yet, it is noteworthy that at higher temperatures or ambient pressure,
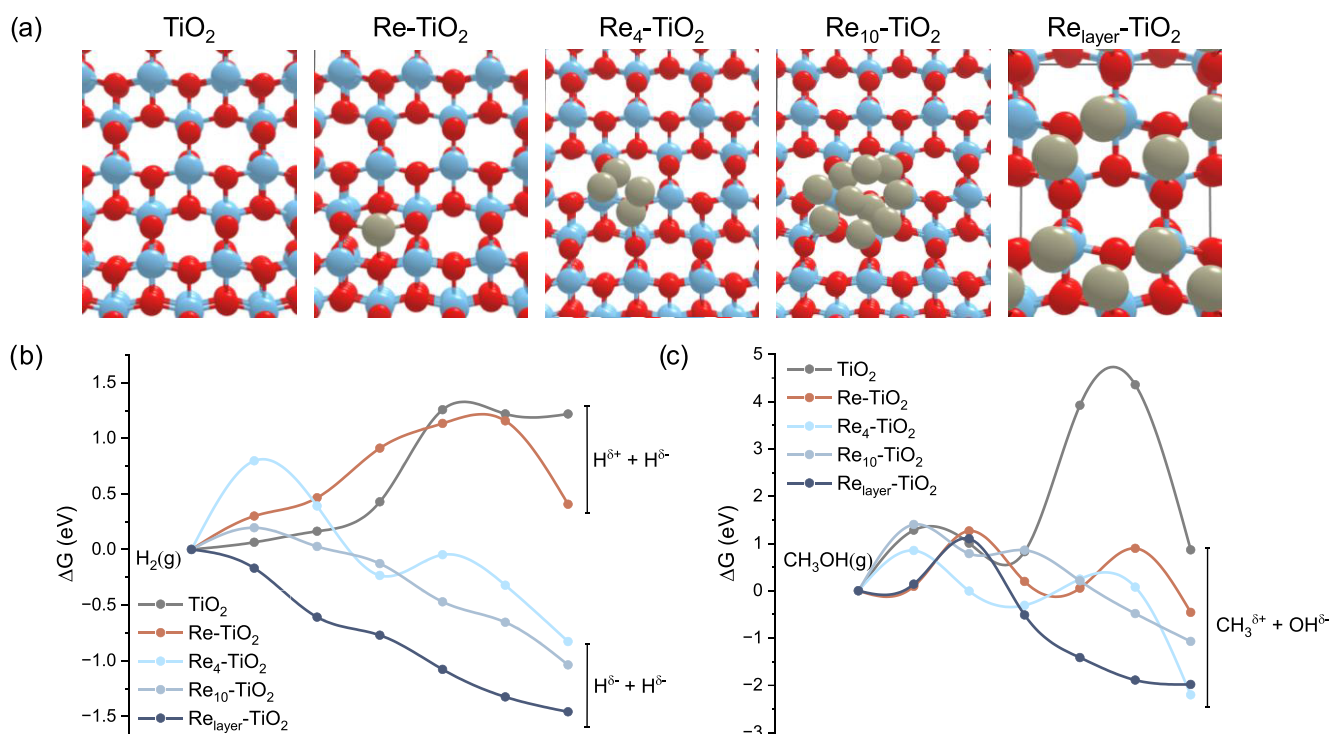
Figure 9. Theoretical models (a) and free energy profiles for the reaction routes of H_2 (b) and CH_3OH (c) dissociation on different model catalysts.

selectivity shifts to CH_4 or CO, respectively, as shown by previous work.[28]

The thermodynamic equilibrium was evaluated through minimization of Gibbs free energy, where H_2, CO_2, CO, CH_3OH, CH_4, and H_2O were considered as components. The CO_2 conversion and selectivities obtained with Aspen Plus showed that, at equilibrium, methane selectivity is >99.9% in all scenarios evaluated, at a pressure range of 1−120 bar, temperature from 150 to 300 °C and CO_2/H_2 ratio of 1:1 through 1:4 and any combination of these variables (Figures S11−S16). This was expected, since methane is the most thermodynamically stable product.[77−81] Based on Le Châtelier's principle, reactions where the number of moles is reduced, such as the production of methanol and methane from the hydrogenation of carbon dioxide, are favored by high pressures.[82−84] Additionally, lower temperatures benefit methane formation as can be seen in Figure 8(a),(b). On the other hand, between 150 and 300 °C, higher temperatures improve the selectivity at thermodynamic equilibrium for methanol and carbon monoxide, as shown in Figure 8(b),(d). Moreover, while increased pressure favors methanol selectivity, it negatively impacts that of carbon monoxide. Although these conditions enhance CO_2 conversion, they also promote methane formation. High pressure and low temperature hinder carbon deposition and favor methanation.[85,86] Despite thermodynamic equilibrium predictions favoring CH_4 formation, the Re/TiO_2 catalyst achieved notable methanol selectivity, particularly at higher GHSV, pressures, and high CO_2 to H_2 ratios such as 1:4 (Figure 7). This difference suggests that the catalyst has a significant influence on directing the reaction selectivity toward CH_3OH, probably because of kinetic constraints in the methanation pathway and the unique active sites offered by Re/TiO_2.

Additionally, Figure 7 shows the CO_2 conversion curves for experimental data and thermodynamic equilibrium considering only methanol as the reaction product. It is noted that the GHSV does not influence the thermodynamic equilibrium since the minimization of Gibbs free energy method does not use information about the interactions of the reactants/ products with the active sites of the catalyst used. In all cases, the theoretical conversion is higher than the experimental one; however, these curves are similar in their behavior, especially for the pressure and ratio (CO_2/H_2) variables. More detailed information about the thermodynamic equilibrium can be found in the Supporting Information.

Theoretical Investigations. To better understand the structure-performance relationship of our TiO_2-supported Re catalysts for CO_2 hydrogenation to methanol, DFT calculations were performed. Five theoretical models were constructed, and two steps of the mechanism were evaluated as previously described by Shen and co-workers for a similar catalyst.[32] The models included a single atom $Re_1/TiO_2(101)$, a four atoms cluster $Re_4/TiO_2(101)$, a ten atoms cluster $Re_{10}/TiO_2(101)$, a Re monolayer (Re_{layer}) covering the $TiO_2(101)$ surface, and the pristine $TiO_2(101)$ surface (Figure 9a for top view and Figure S17 for side view). In all cases, when necessary, the most stable adsorption sites for the rhenium atom, the clusters, or the adsorbates were determined. The optimized geometry revealed Re−O bond lengths ranging from 1.95 to 2.11 Å, with shorter distances associated with $Re_1/TiO_2(101)$ and longer distances linked to $Re_{10}/TiO_2(101)$. These values are similar to those obtained from the best-fit EXAFS models of the reduced Re/TiO_2 samples, which had R values of 2.08 and 2.11 Å for the Re−O bonds when reduced at 250 and 500 °C, respectively. This further indicates the structure of Re/TiO_2 resembles metallic Re nanoclusters in close interaction with the TiO_2 support through O atoms.

Figure S18 shows the electron density difference for all Recontending models. Each case displays distinct chemical environments for electron transfer, indicating variations in the active sites of these catalysts for the reaction.

The first evaluated step of the mechanism of CO_2 conversion to methanol was the dissociation of the hydrogen molecule, which is fundamental to generating adsorbed hydrogen atoms over the surface involved in the reduction steps. The H_2 molecule adsorption starts this step, so the Gibbs free energy of adsorption (ΔG_{ads}) was determined for each model. As shown in Table 1, the H_2 molecule adsorption energy increases from Re_1 to Re_{10} and then shows intermediate values to Re_{layer}, as well as to pristine TiO_2. Such variation of the ΔG_{ads} can be correlated with the coordination number of the rhenium atom. Re_1 with the smaller coordination number exhibits a larger ΔG_{ads}, which can be associated with chemical adsorption, corroborated by the distinct adsorption mode observed (side-on, as shown in Figure S19). This process seems to be like an oxidative addiction to the rhenium atom. For Re_{10} and Re_{layer}, each rhenium atom displays a higher coordination number, and lower values of ΔG_{ads} are observed.

The Gibbs free energy (ΔG) for the H−H dissociation and the activation energy for this reaction were also calculated for each model (see Figures S20 and S21 for product configurations and transition states (TS), respectively). In this case, the importance of rhenium inclusion is demonstrated in the reaction free energy, which is lower in all rhenium-included models than in pristine TiO_2. For this reaction, as the coordination number of rhenium increases, the reaction energy becomes more spontaneous, and the reaction is endergonic only for Re_1. The reason for such a decrease in reaction energy can be suggested by analyzing the charge density differences (Figure S22). For Re_1 and TiO_2, the charge density indicates the formation of $H^{\delta+}$ and $H^{\delta-}$ species, and therefore, the reaction goes through a heterolytic pathway. In both cases, the $H^{\delta+}$ in the products is bonded to an oxygen atom of the surface, and the TS is observed when the hydrogen approaches this atom, requiring a weakening of the Ti−O bond and displaying larger values of E_a (Table 5). On the other hand, the charge densities over the clusters indicate the formation of an $H^{\delta-}-H^{\delta-}$ pair and a homolytic pathway. For these last three models, the TS is observed at the beginning of the reaction coordinate when the dissociation of the H_2 bond starts. For Re_4 and Re_{10}, the E_a shows the same trend as the ΔG_{ads},

indicating a correlation between the coordination number, the amount of charge transferred between the species, and the energy required to break such an interaction partially. For Re_{layer}, the entire dissociation pathway is exergonic.

Subsequently, the H_3C-OH dissociation step was evaluated. In this case, if methanol is formed in the reaction, the desorption energy can be compared to the activation energy of bond dissociation to determine whether the molecule is released or tends to form species like $CH_3^{\delta+}$, which can react and lead to other products, such as CH_4. The ΔG_{ads} of methanol over these models (Figure S23) were obtained and shown in Table 5. The C−O bond dissociation is also endergonic only over pristine TiO_2, while for the other models, an exergonic reaction is observed (see Figure S24 and S25 for products and TS, respectively). Similarly to H_2 dissociation over Re_1 and TiO_2, the positively charged species $CH_3^{\delta+}$ in the products (Figure S26 for charge differences plot) is bonded to oxygen from the TiO_2 surface, and a weakening of the Ti−O bond is required. The E_a energy increases from Re_4 to Re_{10} and then decreases to Re_{layer}. In both Re_4 and Re_{layer}, the dissociation reaction occurs at the top atoms of the cluster or the Re_{layer}. In these cases, the pathway for the charged $CH_3^{\delta+}$ species shows shorter distances to the rhenium atoms compared to Re_{10}, where the path proceeds from the top to the side atoms of the cluster. The interaction of the charged $CH_3^{\delta+}$ species with more rhenium atoms resulted in lower activation energy.

These calculations are in line with the selectivity observed experimentally. The Re_{layer} model is the best fit for 5 wt % rhenium, consistent with nanoparticles of greater than 1 nm on the TiO_2. The Re_{layer} exhibits no barrier to H_2 dissociation and more catalytic sites, in agreement with the higher overall conversion observed for the 5 wt % rhenium material. The largest CH_4 formation, and consequent lowest selectivity to CH_3OH, was observed on the catalyst with the lowest particle size, 1 wt % Re/TiO_2 reduced at 250 °C, which could be related to the simulated Re_4. The dissociation of methanol is spontaneous for all rhenium-containing species, but the most negative values are found for Re_{layer} and Re_4. The desorption of CH_3OH, however, is not spontaneous for Re_4 (as $\Delta G_{desorption} = -\Delta G_{ads}$), therefore leading to a low selectivity. In fact, the highest methanol selectivity is observed for the catalyst with the second smallest size of ~0.6 nm subnanometric Re clusters, 1 wt % Re reduced at 500 °C. In this case, 1 wt % Re/TiO_2 reduced at 500 °C agrees very well with Re_{10}, where the desorption energy of CH_3OH is spontaneous. At the same time, the E_a for C−O bond dissociation for Re_{10} is endergonic, thus indicating that the formed methanol tends to be released instead of forming charged species that can react and lead to other products, which would decrease the methanol yield. For the Re_{layer}, the desorption of methanol occurs spontaneously, and the activation barrier is endergonic. In contrast, the dissociation of methanol in the Re_{layer} is highly exergonic, resulting in the stabilization of the $CH_3^{\delta+}$ species. These stabilized species can then react to enhance the yield of CH_4. This finding is consistent with the observed increase in CH_4 yield when comparing the 5 wt % rhenium catalyst to the 1 wt % rhenium catalyst.

Table 5. Adsorption Free Energy, Dissociation Free Energy, and Activation Barrier for the Models Studied in this Work

	ΔG_{ads} (eV)	$\Delta G_{dissociation}$ (eV)	E_a (eV)
		H_2	
Re_1	−1.55	0.41	1.16
Re_4	−0.61	−0.83	0.80
Re_{10}	0.64	−1.04	0.20
Re_{layer}	0.47	−1.53	0.00
TiO_2	0.61	1.05	1.26
		CH_3OH	
Re_1	0.17	−0.46	1.27
Re_4	−0.24	−2.20	0.85
Re_{10}	1.31	−1.07	1.40
Re_{layer}	1.08	−2.42	1.10
TiO_2	0.16	0.86	4.36

■ CONCLUSION

The Re/TiO_2 catalysts are effective for the hydrogenation of CO_2 to methanol across a wide range of pressures and space

velocities. The synthesis of Re/TiO$_2$ with varied rhenium amounts generates different rhenium species in the as-prepared catalysts, as well as when they are reduced under H$_2$. The lower rhenium loading of 1 wt % results in smaller clusters with stronger interactions with the support, which are subnanometric in size, whereas 5 wt % Re/TiO$_2$ forms particles around 1 nm in diameter. Yet, both 1 and 5 wt % Re/TiO$_2$ present very similar average oxidation states of approximately +1, which is compatible with small metallic Re clusters with interaction to oxygens of the TiO$_2$ support, as shown by bond lengths calculated by DFT and measured by EXAFS. DFT calculations also revealed that the larger the Re cluster size, the lower the energy barriers for H$_2$ activation, in line with the higher conversion rates observed for the larger Re particles. However, the correlation of size and CH$_3$OH selectivity is not straightforward, as the energy of CH$_3$OH dissociation and subsequent hydrogenation to CH$_4$ is lower both over larger **Re$_{layer}$** nanoparticles and over a rather small cluster **Re$_4$**. An optimal cluster size of **Re$_{10}$** leads to a more spontaneous CH$_3$OH desorption and thus higher selectivity. Moreover, the thermodynamics of CO$_2$ hydrogenation are highly selective to CH4, indicating that kinetic effects and catalysis are key factors in methanol synthesis from CO$_2$. At 200 °C, where CH$_4$ formation is kinetically hindered, 1 and 5 wt % Re/TiO$_2$ catalysts were very selective (99 and 97% CH$_3$OH). A slight increase in temperature to 250 °C highlights the effect of Re cluster size, with 5 wt % Re/TiO$_2$ achieving 74% selectivity and 1 wt % Re/TiO$_2$ achieving 97% selectivity to CH$_3$OH. In sum, while a higher rhenium loading will increase the yield of a Re/TiO$_2$ catalyst, adequate cluster sizes are vital for selective methanol production.

■ ASSOCIATED CONTENT

ⓢ Supporting Information

The Supporting Information is available free of charge at https://pubs.acs.org/doi/10.1021/acscatal.5c05984.

> Additional spectra and TEM images for the Re/TiO$_2$ catalysts; detailed methodology for the thermodynamic equilibrium calculations and additional plots; additional images of the theoretical models presented in the DFT study (PDF)

■ AUTHOR INFORMATION

Corresponding Authors

Maite Lippel Gothe − *Departamento de Química Fundamental, Instituto de Química Universidade de São Paulo, São Paulo 05508-000 SP, Brazil;* ◉ orcid.org/0000-0002-7794-665X; Email: maite.gothe@usp.br

Pedro Vidinha − *Departamento de Química Fundamental, Instituto de Química Universidade de São Paulo, São Paulo 05508-000 SP, Brazil;* ◉ orcid.org/0000-0002-3907-4969; Email: pvidinha@iq.usp.br

Authors

Adriano Henrique Braga − *Departamento de Química Fundamental, Instituto de Química Universidade de São Paulo, São Paulo 05508-000 SP, Brazil*

Lais Reis Borges − *Departamento de Química Fundamental, Instituto de Química Universidade de São Paulo, São Paulo 05508-000 SP, Brazil;* ◉ orcid.org/0000-0003-4186-5601

Jiyun Hong − *Stanford Synchrotron Radiation Lightsource, SLAC National Accelerator Laboratory, Menlo Park 94025*

California, United States; ◉ orcid.org/0000-0002-3631-0559

Giliandro Farias − *Instituto de Física, Universidade de São Paulo, São Paulo 05508-090 SP, Brazil*

Alvaro David Torrez Baptista − *Instituto de Física, Universidade de São Paulo, São Paulo 05508-090 SP, Brazil;* ◉ orcid.org/0000-0001-8865-8082

Bryan Alberto Laura Larico − *Departamento de Química Fundamental, Instituto de Química Universidade de São Paulo, São Paulo 05508-000 SP, Brazil*

Ana Barbara Moulin Cansian − *Departamento de Química Fundamental, Instituto de Química Universidade de São Paulo, São Paulo 05508-000 SP, Brazil*

Caetano Rodrigues Miranda − *Instituto de Física, Universidade de São Paulo, São Paulo 05508-090 SP, Brazil*

Simon R. Bare − *Stanford Synchrotron Radiation Lightsource, SLAC National Accelerator Laboratory, Menlo Park 94025 California, United States;* ◉ orcid.org/0000-0002-4932-0342

Liane Marcia Rossi − *Departamento de Química Fundamental, Instituto de Química Universidade de São Paulo, São Paulo 05508-000 SP, Brazil;* ◉ orcid.org/0000-0001-7679-0852

Complete contact information is available at:
https://pubs.acs.org/10.1021/acscatal.5c05984

Notes

The authors declare no competing financial interest.

■ REFERENCES

(1) Olah, G. A. Beyond Oil and Gas: The Methanol Economy. *Angew. Chem., Int. Ed.* **2005**, *44* (18), 2636−2639.

(2) He, X. CO2 Hydrogenation for Ethanol Production: A Thermodynamic Analysis. *Int. J. Oil, Gas. Coal Eng.* **2017**, *5* (6), No. 145.

(3) Reymond, H.; Amado-Blanco, V.; Lauper, A.; von Rohr, P. R. Interplay between Reaction and Phase Behaviour in Carbon Dioxide Hydrogenation to Methanol. *ChemSusChem* **2017**, *10* (6), 1166–1174.

(4) Kommoß, B.; Klemenz, S.; Schmitt, F.; Hocke, E.; Vogel, K.; Drochner, A.; Albert, B.; Etzold, B.; Vogel, H. G. Heterogeneously Catalyzed Hydrogenation of Supercritical CO2 to Methanol. *Chem. Eng. Technol.* **2017**, *40* (10), 1907–1915.

(5) Tidona, B.; Koppold, C.; Bansode, A.; Urakawa, A.; Von Rohr, P. R. CO2 Hydrogenation to Methanol at Pressures up to 950 bar. *J. Supercrit. Fluids* **2013**, *78*, 70–77.

(6) De, S.; Dokania, A.; Ramirez, A.; Gascon, J. Advances in the Design of Heterogeneous Catalysts and Thermocatalytic Processes for CO 2 Utilization. *ACS Catal.* **2020**, *10* (23), 14147–14185.

(7) Zhao, D.; Ortner, N.; Holena, M.; Wohlrab, S.; Kondratenko, E. V. Identifying Catalyst Property Descriptors for CO 2 Hydrogenation to Methanol via Big-Data Analysis. *ACS Catal.* **2023**, *13* (16), 10547–10559.

(8) Ye, J.; Dimitratos, N.; Rossi, L. M.; Thonemann, N.; Beale, A. M.; Wojcieszak, R. Hydrogenation of CO 2 for Sustainable Fuel and Chemical Production. *Science* **2025**, *387* (6737), No. eadn9388.

(9) Zhu, J.; Cannizzaro, F.; Liu, L.; Zhang, H.; Kosinov, N.; Filot, I. A. W.; Rabeah, J.; Brückner, A.; Hensen, E. J. M. Ni–In Synergy in CO 2 Hydrogenation to Methanol. *ACS Catal.* **2021**, *11* (18), 11371–11384.

(10) Wang, J.; Zhang, G.; Zhu, J.; Zhang, X.; Ding, F.; Zhang, A.; Guo, X.; Song, C. CO 2 Hydrogenation to Methanol over In 2 O 3 -Based Catalysts: From Mechanism to Catalyst Development. *ACS Catal.* **2021**, *11* (3), 1406–1423.

(11) Shen, C.; Sun, K.; Zhang, Z.; Rui, N.; Jia, X.; Mei, D.; Liu, C. Highly Active Ir/In 2 O 3 Catalysts for Selective Hydrogenation of CO 2 to Methanol: Experimental and Theoretical Studies. *ACS Catal.* **2021**, *11* (7), 4036–4046.

(12) Dang, S.; Ding, X.; Li, J.; Chang, J.; Zhang, Z.; Gao, P.; Tu, W.; Han, Y. Structure Sensitivity of an Atomic Co-Promoted In 2 O 3 Catalyst toward CO 2 Hydrogenation to Methanol. *ACS Catal.* **2025**, *15* (5), 3967–3979.

(13) Lv, J.; Sun, H.; Liu, G.; Liu, T.; Zhao, G.; Wang, Y.; Tu, X.; Yan, Z. Rational Design of Indium–Palladium Intermetallic Catalysts for Selective CO 2 Hydrogenation to Methanol. *ACS Catal.* **2025**, *15* (1), 23–33.

(14) Jiang, H.; Lin, J.; Wu, X.; Wang, W.; Chen, Y.; Zhang, M. Efficient Hydrogenation of CO2 to Methanol over Pd/In2O3/SBA-15 Catalysts. *J. CO 2 Util.* **2020**, *36*, 33–39.

(15) Broadbent, H. S.; Bartley, W. J. Rhenium Catalysts. VII. Rhenium(VI) Oxide. *J. Org. Chem.* **1963**, *28*, 2345–2347.

(16) Broadbent, H. S. Rhenium and Its Compounds as Hydrogenation Catalysts. *Ann. N. Y. Acad. Sci.* **1967**, *145*, 58–71.

(17) Broadbent, H. S.; Campbell, G. C.; Bartley, W. J.; Johnson, J. H. Rhenium And Its Compounds As Hydrogenation Catalysts. Iii. Rhenium Heptoxide. *J. Org. Chem.* **1959**, *24* (12), 1847–1854.

(18) Figueredo, A. L.; Costa, C. S.; Gothe, M. L.; Rossi, L. M.; Bazito, R. C.; Vidinha, P.; Pereira, C. G. Process Optimization for a Sustainable and Selective Conversion of Fumaric Acid into *γ*-Butyrolactone Over Pd-Re/SiO2. *Catal. Lett.* **2021**, *151* (6), 1821–1833.

(19) Gothe, M. L.; Silva, K. L. C.; Figueredo, A. L.; Fiorio, J. L.; Rozendo, J.; Manduca, B.; Simizu, V.; Freire, R. S.; Garcia, M. A. S.; Vidinha, P. Rhenium − A Tuneable Player in Tailored Hydrogenation Catalysis. *Eur. J. Inorg. Chem.* **2021**, *2021*, No. ejic.202100459.

(20) Costa, C. S.; Figueredo, A. L.; Gothe, M. L.; Bazito, R. C.; Vidinha, P.; Pereira, C. G. A Green Process for High Selective Conversion of *γ*-Butyrolactone into 1,4-Butanediol Using Supercritical CO2. *J. Supercrit. Fluids* **2023**, *199*, No. 105965.

(21) Figueredo, A. L.; Costa, C. S.; Gothe, M. L.; Bazito, R. C.; Vidinha, P.; Pereira, C. G. Tuning the Selectivity of Catalytic

(22) Hydrogenation of Fumaric Acid with Supercritical CO2. *J. Supercrit. Fluids* **2025**, *215*, No. 106424.

(22) Wei, D.; Roisnel, T.; Darcel, C.; Clot, E.; Sortais, J.-B. Hydrogenation of Carbonyl Derivatives with a Well-Defined Rhenium Precatalyst. *ChemCatChem* **2017**, *9* (1), 80–83.

(23) Ly, B. K.; Tapin, B.; Aouine, M.; Delichere, P.; Epron, F.; Pinel, C.; Especel, C.; Besson, M. Insights into the Oxidation State and Location of Rhenium in Re-Pd/TiO2 Catalysts for Aqueous-Phase Selective Hydrogenation of Succinic Acid to 1,4-Butanediol as a Function of Palladium and Rhenium Deposition Methods. *ChemCatChem* **2015**, *7* (14), 2161–2178.

(24) Toyao, T.; Siddiki, S. M. A. H.; Touchy, A. S.; Onodera, W.; Kon, K.; Morita, Y.; Kamachi, T.; Yoshizawa, K.; Shimizu, K. TiO2-Supported Re as a General and Chemoselective Heterogeneous Catalyst for Hydrogenation of Carboxylic Acids to Alcohols. *Chem. - Eur. J.* **2017**, *23* (5), 1001–1006.

(25) Naruto, M.; Agrawal, S.; Toda, K.; Saito, S. Catalytic Transformation of Functionalized Carboxylic Acids Using Multifunctional Rhenium Complexes. *Sci. Rep.* **2017**, *7* (1), No. 3425.

(26) Toyao, T.; Ting, K. W.; Siddiki, S. M. A. H.; Touchy, A. S.; Onodera, W.; Maeno, Z.; Ariga-Miwa, H.; Kanda, Y.; Asakura, K.; Shimizu, K. Mechanistic Study of the Selective Hydrogenation of Carboxylic Acid Derivatives over Supported Rhenium Catalysts. *Catal. Sci. Technol.* **2019**, *9* (19), 5413–5424.

(27) Tomishige, K.; Nakagawa, Y.; Tamura, M. Taming Heterogeneous Rhenium Catalysis for the Production of Biomass-Derived Chemicals. *Chin. Chem. Lett.* **2019**, *31* (5), 1071–1077.

(28) Gothe, M. L.; Pérez-Sanz, F. J.; Braga, A. H.; Borges, L. R.; Abreu, T. F.; Bazito, R. C.; Gonçalves, R. V.; Rossi, L. M.; Vidinha, P. Selective CO2 Hydrogenation into Methanol in a Supercritical Flow Process. *J. CO 2 Util.* **2020**, *40*, No. 101195.

(29) Machado, F.; Gothe, L.; Reis Borges, L.; Portes, M. C.; Rodrigues, O.; Ando, R. A.; Rossi, L. M.; Vidinha, P.; Gothe, M. L.; Borges, L. R.; Portes, M. C.; Ando, R. A.; Rossi, L. M. Unveiling the Role of Rhenium Precursors in Supercritical CO2 Hydrogenation: A Comparative Study of ReOx/TiO2 Catalysts. *ChemCatChem* **2025**, No. e202401874.

(30) Tang, S.; Feng, Z.; Han, Z.; Sha, F.; Tang, C.; Zhang, Y.; Wang, J.; Li, C. Mononuclear Re Sites on In2O3 Catalyst for Highly Efficient CO2 Hydrogenation to Methanol. *J. Catal.* **2023**, *417*, 462–472.

(31) Phongprueksathat, N.; Ting, K. W.; Mine, S.; Jing, Y.; Toyoshima, R.; Kondoh, H.; Shimizu, K.; Toyao, T.; Urakawa, A. Bifunctionality of Re Supported on TiO2 in Driving Methanol Formation in Low-Temperature CO2 Hydrogenation. *ACS Catal.* **2023**, *13* (16), 10734–10750.

(32) Shen, C.; Sun, K.; Zou, R.; Wu, Q.; Mei, D.; Liu, C. CO2 Hydrogenation to Methanol on Indium Oxide-Supported Rhenium Catalysts: The Effects of Size. *ACS Catal.* **2022**, *12* (20), 12658–12669.

(33) Gili, A.; Brösigke, G.; Javed, M.; Dal Molin, E.; Isbrücker, P.; Repke, J. U.; Hess, F.; Gurlo, A.; Schomäcker, R.; Bekheet, M. F. Performance and Stability of Corundum-Type In2O3 Catalyst for Carbon Dioxide Hydrogenation to Methanol. *Angew. Chem., Int. Ed.* **2025**, *64* (5), No. e202416990.

(34) Sreenithya, A.; Kolganov, A. A.; Yeu, I. W.; Risansyauqi, M. H.; Pidko, E. A. Oxidation State of Single-Atom Re/TiO 2 Hydrogenation Catalysts: A Computational Study. *ACS Catal.* **2024**, *14* (24), 18488–18498.

(35) Zhou, C.; Aitbekova, A.; Liccardo, G.; Oh, J.; Stone, M. L.; McShane, E. J.; Werghi, B.; Nathan, S.; Song, C.; Ciston, J.; Bustillo, K. C.; Hoffman, A. S.; Hong, J.; Perez-Aguilar, J.; Bare, S. R.; Cargnello, M. Steam-Assisted Selective CO 2 Hydrogenation to Ethanol over Ru–In Catalysts. *Angew. Chem., Int. Ed.* **2024**, *63* (41), No. e202406761, DOI: 10.1002/anie.202406761.

(36) Ye, R.; Ma, L.; Hong, X.; Reina, T. R.; Luo, W.; Kang, L.; Feng, G.; Zhang, R.; Fan, M.; Zhang, R.; Liu, J. Boosting Low-Temperature CO2 Hydrogenation over Ni-Based Catalysts by Tuning Strong Metal-Support Interactions. *Angew. Chem., Int. Ed.* **2024**, *63* (3), No. e202317669, DOI: 10.1002/anie.202317669.

(37) Wang, C.; Jin, Z.; Guo, L.; Yamamoto, O.; Kaida, C.; He, Y.; Ma, Q.; Wang, K.; Tsubaki, N. New Insights for High-Through CO$_2$ Hydrogenation to High-Quality Fuel. *Angew. Chem., Int. Ed.* **2024**, *63*, No. e202408275, DOI: 10.1002/anie.202408275.

(38) Wu, W.; Wang, Y.; Luo, L.; Wang, M.; Li, Z.; Chen, Y.; Wang, Z.; Chai, J.; Cen, Z.; Shi, Y.; Zhao, J.; Zeng, J.; Li, H. CO2 Hydrogenation over Copper/ZnO Single-Atom Catalysts: Water-Promoted Transient Synthesis of Methanol. *Angew. Chem., Int. Ed.* **2022**, *61* (48), No. e202213024.

(39) Hu, X.; Xu, D.; Jiang, J. Strong Metal-Support Interaction between Pt and TiO2 over High-Temperature CO2 Hydrogenation. *Angew. Chem.* **2025**, *137* (7), No. e202419103.

(40) Hoffman, A. S.; Singh, J. A.; Bent, S. F.; Bare, S. R.; et al. In Situ Observation of Phase Changes of a Silica-Supported Cobalt Catalyst for the Fischer−Tropsch Process by the Development of a Synchrotron-Compatible *in Situ/Operando* Powder X-Ray Diffraction Cell. *J. Synchrotron Radiat.* **2018**, *25* (6), 1673−1682.

(41) Perry, R. H. G. Perry's Chemical Engineers' Handbook (7th Edition), McGraw-Hill *J. Chem. Educ.* 1997.

(42) Stangeland, K.; Li, H.; Yu, Z. Thermodynamic Analysis of Chemical and Phase Equilibria in CO2 Hydrogenation to Methanol, Dimethyl Ether, and Higher Alcohols. *Ind. Eng. Chem. Res.* **2018**, *57* (11), 4081−4094.

(43) Mathias, P. M. A Versatile Phase Equilibrium Equation of State. *Ind. Eng. Chem. Process Des. Dev.* **1983**, *22* (3), 385−391.

(44) Bennekom, J. G. v.; Winkelman, J. G. M.; Venderbosch, R. H.; Nieland, S. D. G. B.; Heeres, H. J. Modeling and Experimental Studies on Phase and Chemical Equilibria in High-Pressure Methanol Synthesis. *Ind. Eng. Chem. Res.* **2012**, *51* (38), 12233−12243.

(45) Kresse, G.; Furthmüller, J. Efficient Iterative Schemes for *Ab Initio* Total-Energy Calculations Using a Plane-Wave Basis Set. *Phys. Rev. B* **1996**, *54* (16), No. 11169.

(46) Perdew, J. P.; Burke, K.; Ernzerhof, M. Generalized Gradient Approximation Made Simple. *Phys. Rev. Lett.* **1996**, *77* (18), No. 3865.

(47) Kresse, G.; Joubert, D. From Ultrasoft Pseudopotentials to the Projector Augmented-Wave Method. *Phys. Rev. B* **1999**, *59* (3), No. 1758.

(48) Henkelman, G.; Uberuaga, B. P.; Jónsson, H. A Climbing Image Nudged Elastic Band Method for Finding Saddle Points and Minimum Energy Paths. *J. Chem. Phys.* **2000**, *113* (22), 9901−9904.

(49) Henkelman, G.; Jónsson, H. Improved Tangent Estimate in the Nudged Elastic Band Method for Finding Minimum Energy Paths and Saddle Points. *J. Chem. Phys.* **2000**, *113* (22), 9978−9985.

(50) Okal, J. A Study of Effect of Particle Size on the Oxidation of Rhenium in the Re/γ-Al2O3 Catalysts. *Appl. Catal., A* **2005**, *287* (2), 214−220.

(51) Okal, J.; Tylus, W.; Kępiński, L. XPS Study of Oxidation of Rhenium Metal on γ-Al2O3 Support. *J. Catal.* **2004**, *225* (2), 498−509.

(52) Okal, J.; Kępiński, L.; Krajczyk, L.; Drozd, M. Oxidation and Redispersion of a Re/γ-Al2O3 Catalyst. *J. Catal.* **1999**, *188* (1), 140−153.

(53) Okal, J.; Baran, J. Laser Raman Characterization of Oxidized Re/γ-Al2O3 Catalysts: Effect of Calcination Temperature. *J. Catal.* **2001**, *203* (2), 466−476.

(54) Andriopoulou, C.; Boghosian, S. Heterogeneity of Deposited Phases in Supported Transition Metal Oxide Catalysts: Reversible Temperature-Dependent Evolution of Molecular Structures and Configurations. *Phys. Chem. Chem. Phys.* **2018**, *20* (3), 1742−1751.

(55) Vuurman, M. A.; Stufkens, D. J.; Oskam, A.; Wachs, I. E. Structural Determination of Surface Rhenium Oxide on Various Oxide Supports (Al2O3, ZrO2, TiO2 and SiO2). *J. Mol. Catal.* **1992**, *76* (1−3), 263−285.

(56) Wang, L.; Hall, W. K. The Preparation and Properties of Rhenia-Alumina Catalysts. *J. Catal.* **1983**, *82* (1), 177−184.

(57) Hardcastle, F. D.; Wachs, I. E.; Horsley, J. A.; Via, G. H. The Structure of Surface Rhenium Oxide on Alumina from Laser Raman Spectroscopy and X-Ray Absorption near-Edge Spectroscopy. *J. Mol. Catal.* **1988**, *46* (1−3), 15−36.

(58) Purans, J.; Kuzmin, A.; Cazzanelli, E.; Mariotto, G. Disorder-Induced Raman Scattering in Rhenium Trioxide (ReO$_3$. *J. Phys.: Condens. Matter* **2007**, *19* (22), No. 226206.

(59) Wu, Y.; Holdren, S.; Zhang, Y.; Oh, S. C.; Tran, D. T.; Emdadi, L.; Lu, Z.; Wang, M.; Woehl, T. J.; Zachariah, M.; Lei, Y.; Liu, D. Quantification of Rhenium Oxide Dispersion on Zeolite: Effect of Zeolite Acidity and Mesoporosity. *J. Catal.* **2019**, *372*, 128−141.

(60) Mitra, B.; Gao, X.; Wachs, I. E.; Hirt, A. M.; Deo, G. Characterization of Supported Rhenium Oxide Catalysts: Effect of Loading, Support and Additives. *Phys. Chem. Chem. Phys.* **2001**, *3* (6), 1144−1152.

(61) Iqbal, S.; Shozi, M. L.; Morgan, D. J. X-ray Induced Reduction of Rhenium Salts and Supported Oxide Catalysts. *Surf. Interface Anal.* **2017**, *49* (3), 223−226.

(62) Hofmann, B. J. High Valent Rhenium Compounds in Catalysis: Synthesis, Reactivity and Decomposition Pathways, Ph.D. Thesis; Natural Sciences, Technischen Universität München, 2021.

(63) Toyao, T.; Siddiki, S. M. A. H.; Morita, Y.; Kamachi, T.; Touchy, A. S.; Onodera, W.; Kon, K.; Furukawa, S.; Ariga, H.; Asakura, K.; Yoshizawa, K.; Shimizu, K. Rhenium-Loaded TiO2: A Highly Versatile and Chemoselective Catalyst for the Hydrogenation of Carboxylic Acid Derivatives and the N-Methylation of Amines Using H 2 and CO 2. *Chem. - Eur. J.* **2017**, *23* (59), 14848−14859.

(64) Crist, B. V. *Monochromatic XPS Spectra Commercially Pure Binary Oxides*; XPS International, LLC: Salem, Oregon, USA, 2019.

(65) Greiner, M. T.; Rocha, T. C. R.; Johnson, B.; Klyushin, A.; Knop-Gericke, A.; Schlögl, R. The Oxidation of Rhenium and Identification of Rhenium Oxides during Catalytic Partial Oxidation of Ethylene: An in-Situ Xps Study. *Z. Phys. Chem.* **2014**, *228* (4−5), 521−541.

(66) Avramescu, S.; Ene, C. D.; Ciobanu, M.; Schnee, J.; Devred, F.; Bucur, C.; Vasile, E.; Colaciello, L.; Richards, R.; Gaigneaux, E. M.; Verziu, M. N. Nanocrystalline Rhenium-Doped TiO2: An Efficient Catalyst in the One-Pot Conversion of Carbohydrates into Levulinic Acid. the Synergistic Effect between Brønsted and Lewis Acid Sites. *Catal. Sci. Technol.* **2022**, *12* (1), 167−180.

(67) Mine, S.; Ting, K. W.; Li, L.; Hinuma, Y.; Maeno, Z.; Siddiki, S. M. A. H.; Toyao, T.; Shimizu, K. Experimental and Theoretical Investigation of Metal−Support Interactions in Metal-Oxide-Supported Rhenium Materials. *J. Phys. Chem. C* **2022**, *126* (9), 4472−4482.

(68) Bare, S. R.; Kelly, S. D.; D Vila, F.; Boldingh, E.; Karapetrova, E.; Kas, J.; Mickelson, G. E.; Modica, F. S.; Yang, N.; Rehr, J. J. Experimental (XAS, STEM, TPR, and XPS) and Theoretical (DFT) Characterization of Supported Rhenium Catalysts. *J. Phys. Chem. C* **2011**, *115* (13), 5740−5755.

(69) Naumov, A. V. Rhythms of Rhenium. *Russ. J. Non-Ferrous Met.* **2007**, *48* (6), 418−423.

(70) Yang, B.; Wang, Y.; Gao, B.; Zhang, L.; Guo, L. Size-Dependent Active Site and Its Catalytic Mechanism for CO2 Hydrogenation Reactivity and Selectivity over Re/TiO2. *ACS Catal.* **2023**, *13* (15), 10364−10374.

(71) Ting, K. W.; Mine, S.; Ait El Fakir, A.; Du, P.; Li, L.; Siddiki, S. M. A. H.; Toyao, T.; Shimizu, K. The Reducibility and Oxidation States of Oxide-Supported Rhenium: Experimental and Theoretical Investigations. *Phys. Chem. Chem. Phys.* **2022**, *24* (46), 28621−28631.

(72) Yang, B.; Gao, B.; Wang, Y.; Mou, J.; Zhang, L.; Guo, L. Identification of the Active Sites for CO2Methanation over Re/TiO2 Catalysts. *J. Catal.* **2024**, *432*, No. 115464.

(73) Greenler, R. G.; Burch, K. D.; Kretzschmar, K.; Klauser, R.; Bradshaw, A. M.; Hayden, B. E. Stepped Single-Crystal Surfaces as Models for Small Catalyst Particles. *Surf. Sci.* **1985**, *152−153*, 338−345.

(74) Hollins, P. The Influence of Surface Defects on the Infrared Spectra of Adsorbed Species. *Surf. Sci. Rep.* **1992**, *16* (2), 51−94.

(75) Morris, R. H. Estimating the Wavenumber of Terminal Metal-Hydride Stretching Vibrations of Octahedral d^6 Transition Metal Complexes. *Inorg. Chem.* **2018**, *57* (21), 13809−13821.

(76) Cho, H.-G.; Andrews, L. Formation of HC⫶ReH$_3$ in Methane Activation by Rhenium Atoms: Observation of the Elusive Methylidyne C−H Stretching Absorption. *Organometallics* **2007**, *26* (17), 4098−4101.

(77) Smith, J. M.; Van Ness, H. C.; Abbott, M. M.; Swihart, M. T. *Introduction to Chemical Engineering Thermodynamics*; McGraw-Hill Education, 2018.

(78) Ahmad, K.; Upadhyayula, S. Greenhouse Gas CO2 Hydrogenation to Fuels: A Thermodynamic Analysis. *Environ. Prog. Sustainable Energy* **2019**, *38* (1), 98−111.

(79) Jia, C.; Gao, J.; Dai, Y.; Zhang, J.; Yang, Y. The Thermodynamics Analysis and Experimental Validation for Complicated Systems in CO2 Hydrogenation Process. *J. Energy Chem.* **2016**, *25* (6), 1027−1037.

(80) da S Bronsato, B. J. Hydrogenation of CO2 to Methanol: The Role of Oxygen Vacancies in Methanol Using Cu/ZnO/Al Catalysts and In2O3-Based Mixtures, Ph.D. Thesis; Chemical Engineering, Pontifícia Universidade: Católica do Rio de Janeiro, Rio de Janeiro, 2023.

(81) Goodwin, A. R. H.; Sengers, J. V.; Peters, C. J. *Applied Thermodynamics of Fluids*; RSC Publishing: Cambridge, 2010.

(82) Ott, J. B.; Boerio-Goates, J. *Chemical Thermodynamics. [Vol. 1], Principles and Applications*; Academic, 2000.

(83) Atkins, P. W.; De Paula, J.; Keeler, J. *Atkins' Physical Chemistry*, 12th ed.; Oxford University Press: Oxford, 2023.

(84) Kanuri, S.; Roy, S.; Chakraborty, C.; Datta, S. P.; Singh, S. A.; Dinda, S. An Insight of CO2 Hydrogenation to Methanol Synthesis: Thermodynamics, Catalysts, Operating Parameters, and Reaction Mechanism. *Int. J. Energy Res.* **2022**, *46* (5), 5503−5522.

(85) Ghaib, K.; Nitz, K.; Ben-Fares, F. Z. Chemical Methanation of CO2: A Review. *ChemBioEng Rev.* **2016**, *3* (6), 266−275.

(86) Gao, J.; Wang, Y.; Ping, Y.; Hu, D.; Xu, G.; Gu, F.; Su, F. A Thermodynamic Analysis of Methanation Reactions of Carbon Oxides for the Production of Synthetic Natural Gas. *RSC Adv.* **2012**, *2* (6), 2358−2368.